

Ocean–Atmosphere Interaction over Agulhas Extension Meanders

W. TIMOTHY LIU AND XIAOSU XIE

Jet Propulsion Laboratory, California Institute of Technology, Pasadena, California

PEARN P. NILER

Scripps Institute of Oceanography, La Jolla, California

(Manuscript received 18 October 2006, in final form 15 March 2007)

ABSTRACT

Many years of high-resolution measurements by a number of space-based sensors and from Lagrangian drifters became available recently and are used to examine the persistent atmospheric imprints of the semipermanent meanders of the Agulhas Extension Current (AEC), where strong surface current and temperature gradients are found. The sea surface temperature (SST) measured by the Advanced Microwave Scanning Radiometer–Earth Observing System (AMSR-E) and the chlorophyll concentration measured by the Sea-viewing Wide Field-of-view Sensor (SeaWiFS) support the identification of the meanders and related ocean circulation by the drifters. The collocation of high and low magnitudes of equivalent neutral wind (ENW) measured by Quick Scatterometer (QuikSCAT), which is uniquely related to surface stress by definition, illustrates not only the stability dependence of turbulent mixing but also the unique stress measuring capability of the scatterometer. The observed rotation of ENW in opposition to the rotation of the surface current clearly demonstrates that the scatterometer measures stress rather than winds. The clear differences between the distributions of wind and stress and the possible inadequacy of turbulent parameterization affirm the need of surface stress vector measurements, which were not available before the scatterometers. The opposite sign of the stress vorticity to current vorticity implies that the atmosphere spins down the current rotation through momentum transport. Coincident high SST and ENW over the southern extension of the meander enhance evaporation and latent heat flux, which cools the ocean. The atmosphere is found to provide negative feedback to ocean current and temperature gradients. Distribution of ENW convergence implies ascending motion on the downwind side of local SST maxima and descending air on the upwind side and acceleration of surface wind stress over warm water (deceleration over cool water); the convection may escalate the contrast of ENW over warm and cool water set up by the dependence of turbulent mixing on stability; this relation exerts a positive feedback to the ENW–SST relation. The temperature sounding measured by the Atmospheric Infrared Sounder (AIRS) is consistent with the spatial coherence between the cloud-top temperature provided by the International Satellite Cloud Climatology Project (ISCCP) and SST. Thus ocean mesoscale SST anomalies associated with the persistent meanders may have a long-term effect well above the midlatitude atmospheric boundary layer, an observation not addressed in the past.

1. Introduction

The ocean has a long memory and its feedback to the atmosphere governs climate changes. The coupling of the small and slow processes of the ocean to the transient and large-scale processes of the atmosphere, particularly in the extratropical latitudes and for long time

periods, has been controversial. Over the global ocean, areas associated with ocean fronts are particularly interesting, because they have extremely high mean kinetic energy, and the smaller-scale variation of wind convergence and evaporation may produce localized buoyancy and energetic vertical motion that could propagate the ocean effects far up into the atmosphere.

Active air–sea coupling across ocean fronts has been known, particularly on short time scales. It was demonstrated in a number of field campaigns, including the Joint Air–Sea Interaction experiment (JASIN) in the North Sea in the summer of 1978 (e.g., Guymer et al.

Corresponding author address: W. Timothy Liu, Jet Propulsion Laboratory, MS 300-323, California Institute of Technology, Pasadena, CA 91109-8001.
E-mail: liu@pacific.jpl.nasa.gov

1983), the Equatorial Pacific Ocean Climate Studies (EPOCS) in the eastern equatorial Pacific in the winter of 1980 (e.g., Greenhut 1982), and the Frontal Air–Sea Interaction Experiment (FASINEX; e.g., Friehe et al. 1991). The results show coupling mainly within the atmospheric boundary layer.

There have been many studies on large-scale coupling and long-term climate changes based on numerical model simulation and analysis of model products (e.g., Lau and Nath 1994; Kushnir et al. 2002; Liu and Wu 2004). Because of the strong effort to understand El Niño and Southern Oscillation in the past few decades, ocean–atmosphere coupling in the tropics and subtropics is relatively better understood through observations. Space observations have made contributions in momentum (e.g., Liu et al. 1996) and heat (e.g., Liu et al. 1994) balances. Liu and Xie (2002), in their study of double intertropical convergence zone (ITCZ), presented observational evidence of two major mechanisms by which the ocean drives the atmosphere. When the ocean is warm and SST is above the deep convection threshold (around 26°–27°C), as associated with the stronger ITCZ, surface winds from different directions converge to the local SST maximum, driven by the pressure gradient force. The weaker ITCZ occurs over cooler water and is caused by the deceleration of the surface winds as they approach the cold upwelling water near the equator. Decreases in turbulent mixing and increases in vertical wind shear over cooler water are suggested to be the causes. The hypothesis was supported by Luis and Pandey (2005) in the analysis over the Indian Ocean. If the hypothesis is correct the stability mechanism should prevail over a large part of the global ocean (where SST < 26°C), as reviewed by Xie (2004). The two mechanisms (pressure gradient and turbulent mixing) will cause different phase relationships between surface stress and SST (e.g., Hayes et al. 1989).

The recent availability of space-based high-resolution ocean surface wind stress (as reviewed by Liu 2002 and Liu and Xie 2006) and SST (e.g., Wentz et al. 2000) induced many investigations on the coherence of ocean and atmosphere features. Many investigators have described the coherent propagation of Quick Scatterometer (QuikSCAT) measurements and the thermal front of tropical instability waves (TIW; e.g., Xie et al. 1998; Liu et al. 2000; Wentz et al. 2000) have postulated the boundary layer mechanisms behind the coherence propagations (e.g., Chelton et al. 2001; Hashizume et al. 2002; Cronin et al. 2003) and have simulated the coupling in numerical models (e.g., Yu and Liu 2003; Small et al. 2003; Song et al. 2004). The coherent features were also observed over extratropical SST fronts (Xie

et al. 2002; White and Annis 2003; Nonaka and Xie 2003; O’Neill et al. 2005) in the Indian Ocean (Vecchi et al. 2004), over the Gulf Stream rings (Park and Cornillon 2002), and in the wake of tropical cyclones (Lin et al. 2003). Scatterometer features associated with the horizontal shear zone of ocean current were also observed by Cornillon and Park (2001) over Gulf Stream rings, by Kelly et al. (2001) over equatorial current, and by Polito et al. (2001) over TIW. Because QuikSCAT observed an in-phase relation between the horizontal variations of stress and SST, there should be an in-phase relation between stress vorticity and cross-wind SST gradient, as demonstrated by Chelton et al. (2001, 2004) and O’Neill et al. (2003, 2005). The SST-generated vorticity (curl) of wind stress may in turn drive ocean circulation as postulated by White and Annis (2003).

Wind stress or air–sea momentum flux (τ) has been directly measured only in limited regions over limited time. Until the launch of the scatterometer, our knowledge of τ distribution is largely derived from winds measured at ships and buoys through a drag coefficient (turbulence parameterization). As described in section 2, τ is the turbulent transfer of momentum, and turbulence is generated by instability of the atmosphere caused both by wind shear (difference between wind and current) and buoyancy (density stratification resulted from vertical temperature and humidity gradients). Thus, over the strong horizontal temperature and current gradients of the ocean fronts, the distribution of τ is very different from the overlying winds. Although it is generally recognized that scatterometers measure stress, the correlation between scatterometer observations and ocean parameters are often discussed in terms of wind errors or wind anomalies because of insufficient understanding of the characteristics of stress.

In this study, the characteristics of momentum exchanges will be demonstrated over the Agulhas Extension Current (AEC) meanders also known as Agulhas Return Current, where the frontal meanders are semi-permanent. Possible extension of the ocean influence beyond the turbulent atmospheric boundary layer will also be described. The scope of this study is limited to what our measurements reveal, as described in section 3. The implications of the observation, particularly of the feedback mechanism, and the scientific questions raised are discussed in section 4.

2. Data

a. Scatterometer

The scatterometer sends microwave pulses to the earth’s surface and measures the backscatter power.

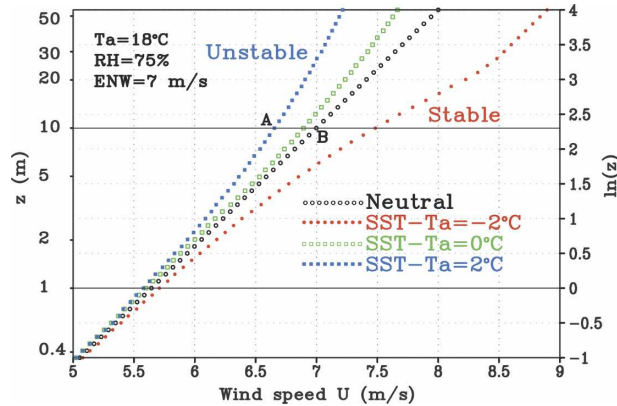


FIG. 1. Typical wind profiles at various stability conditions derived from the flux-profile relation by Liu et al. (1979). Here B is the equivalent neutral wind corresponding to the actual wind measurement at A.

Over the ocean, the backscatter power is largely caused by small centimeter-scale waves on the surface, which are believed to be in equilibrium with τ . Liu and Large (1981) demonstrated, for the first time, the relation between measurements by a space-based scatterometer and surface stress measured on research ships. The geophysical data product of the scatterometer is the equivalent neutral wind (ENW) at a reference level (Liu and Tang 1996), which, by definition, is uniquely related to τ , while the relation between τ and the actual winds (u) at the reference level depends on atmosphere stability and ocean surface current.

Surface stress is transported by chaotic turbulence. The expression of turbulence in terms of stability parameters, such as Richardson number or Obukhov length, has been described in textbooks (e.g., Fleagle and Businger 1963; Tennekes and Lumley 1972). The relation between τ and u at a height of z , in terms of an empirical drag coefficient (C_D), has been studied extensively and is governed by the flux-profile relation (e.g., Liu et al. 1979):

$$\frac{u - u_s}{u_*} = 2.5 \left(\ln \frac{z}{z_0} - \psi_u \right) = \frac{1}{\sqrt{C_D}}, \quad (1)$$

where u_s is the surface current, $u_* = (\tau/\rho)^{1/2}$ is the frictional velocity, ρ is the air density, z_0 is roughness length, and ψ is the function of the stability parameter. The stability parameter is the ratio of buoyancy to shear production of turbulence. Typical wind profiles at various stabilities are shown in Fig. 1 as an illustration. The stress or u_* is related to the vertical wind shear (the vector difference between wind and surface current), not just the wind vector. ENW, similar to the frictional velocity, can be viewed as stress scaled to the wind unit.

The effect of sea state and surface waves (Geernart 1990) are not included explicitly in the relation.

Advection, rolls (secondary flow), organized convection, and cloud entrainment, affect boundary layer dynamics and winds, but their effects on τ have to be manifested through surface turbulence and Eq. (1) (e.g., Brown and Liu 1982). Liu and Tang (1996) described the method of computing ENW from conventional measurements of winds at buoys and ships, which are made within the lowest 50 m of the boundary layer where more complicated factors (e.g., flux divergence, baroclinicity, Coriolis force) do not significantly affect turbulent mixing and the drag coefficient. This method has been used in calibration/validation of measurements for all the scatterometers launched by the National Aeronautics and Space Administration (NASA), starting with *Seasat* in 1978. An example is illustrated in Fig. 1. Starting with in situ measurements made under unstable conditions (A on blue curve), u_* and z_0 are computed from the curve (the gradient and intercept at the surface) defined by the flux-profile relation of Liu et al. (1979). With u_* and z_0 , we move up the neutral profile (black straight line) to B to get ENW at the reference height (10 m). As discussed by Liu and Tang (1996) and shown in Fig. 1, ENW is higher than u under unstable conditions and lower than u under stable conditions.

b. Other data

Recently, more than a decade long of global dataset of near-surface current has been made available. The current velocity was derived from Argos satellite collections of the displacements of drifters with drogues centered at 15-m depth (Niiler 2001). Five years of data from January 2000 to December 2004 were averaged and used in this study.

The Advanced Microwave Scanning Radiometer-Earth Observing System (AMSR-E), on board NASA's *Aqua* satellite, was launched in May 2002 and has been collecting global hydrological parameters. Over the ocean, a number of parameters, including SST, precipitable water (W), and wind speed, have been derived from AMSR-E. These three parameters averaged to 0.25° by 0.25° grids for ascending and descending paths (Wentz and Meissner 2000), were obtained from Remote Sensing System. They were averaged daily and used to compute latent heat flux (LH) based on the methodology by Liu et al. (1991, 1994). Both the SST and LH were then averaged between June 2002 and December 2004.

The chlorophyll concentration was derived from Sea-viewing Wide Field-of-view Sensor (SeaWiFS) level-3

monthly maps with a 9-km resolution (McClain et al. 2004) from the Goddard Space Flight Center (GSFC) and was gridded to 0.5° by 0.5° and averaged from January 2000 to December 2004 in this study.

Atmospheric Infrared Sounder (AIRS) has provided temperature and humidity profiles in the atmosphere with accuracy comparable to those of conventional radiosondes since 2002 (Chahine et al. 2006). Temperatures at 12 levels from 1000 to 100 mb from September 2002 to December 2004 from the GSFC Data Active Archive Center have been averaged and used in this study.

The International Satellite Cloud Climatology Project (ISCCP; Rossow and Schiffer 1999) high-resolution dataset, known as ISCCP DX, was used. This data consists of samples at 30 km resolution and 3 hr time intervals. ISCCP provides data from all operational geostationary and polar-orbiting weather satellites, but only Meteosat-5 data were used in this study. They are provided at the Langley Research Center Atmospheric Science Data Center. Cloud-top temperature (CTT), cloud flag pixel, and cloud optical thickness from January 2000 to December 2004 are examined.

The operational numerical weather prediction (NWP) analysis products of the National Centers for Environmental Prediction (NCEP) at 1° resolution for the 5-yr period were obtained from the National Center for Atmospheric Research. The high-resolution surface wind vectors (at 1°) and the temperature and humidity soundings (at 0.5°) of the European Centre for Medium-Range Weather Forecasts (ECMWF) were obtained for the same periods by the QuikSCAT and AIRS projects for validation purposes under special arrangements.

c. Isolating the signal

To separate the features related to AEC meanders from the large-scale spatial gradients, a two-dimensional filter was applied to the monthly mean of all parameters. The filter essentially removed the running mean with scales of 10° in longitude and 2° in latitude, weighted by a sine function. The deviations from the running mean were averaged through the available data period to construct the long-term mean anomalies; they are referred to anomalies hereafter. The circular anomaly features associated with the AEC meanders are referred to as eddies. For the zonal (U) and meridional (V) components of a vector (ENW or surface current), the convergence ($-\partial U/\partial x - \partial V/\partial y$) and vorticity ($\partial V/\partial x - \partial U/\partial y$) anomalies are computed from the 5-yr means of U and V anomalies. Vorticity is the vertical component of the curl of the vector.

3. Results

a. Current

The drifters reveal the semipermanent meanders of the AEC extending from the southern tip of the African continent east into the Indian Ocean. Figure 2 shows that the strongest part of the current is located approximately at 39°S , and the magnitude of the 5-yr mean reaches about 0.6 m s^{-1} . High chlorophyll, as measured by SeaWiFS, and cold SST, as measured by AMSR-E, are located with the cyclonic (clockwise in the Southern Hemisphere) current; warm SST and low chlorophyll are located with anticyclonic currents. Very high chlorophyll is also found poleward of the strongest zonal current.

Cyclonic currents cause divergence and the upwelling of cold and nutrient rich water, and anticyclonic currents cause convergence and downwelling, in agreement with the basic geophysical fluid dynamics. Such a scenario is more clearly exhibited after the filtering (described in section 2c), as shown in Figs. 3 and 4a. Although SST data are averaged only over a 3-yr period, while chlorophyll and surface current are averaged over a 5-yr period, the centers of SST anomalies (Fig. 3b) are collocated with centers of chlorophyll (Fig. 3a), except for slight shifts (e.g., at 45° and 53°E). The chlorophyll and SST anomalies are also collocated with current vorticity anomalies (Fig. 4a), except at 45° and 53.5°E , where the vorticity centers are ill defined. Drifter data are sparse and it takes a few years to cover the region fully. Space-based measurements of SST and chlorophyll serve to support the location of the eddies by the drifters.

b. Current effect on stress

The mean ENW measured by QuikSCAT are westerly, reaching over 7 m s^{-1} over the AEC. With the large-scale zonal means removed by the same filter as used for the currents, the ENW anomalies (Fig. 4b) show rotations in opposite direction to the current anomalies (Fig. 4a) at most locations, most clearly at 25° and 30°E . The opposite rotation centers are slightly shifted at other locations or less clearly defined at 35° and 54°E . Although the mean ENW is more than 10 times stronger than the mean current, the vorticity of the current is stronger than that of the ENW. The opposite rotation of ENW with respect to the current implies that the scatterometer measures surface stress rather than wind as explained in section 2a.

c. Temperature effect on stress

The collocation of and the positive correlation between the magnitude of ENW (or τ) and SST are

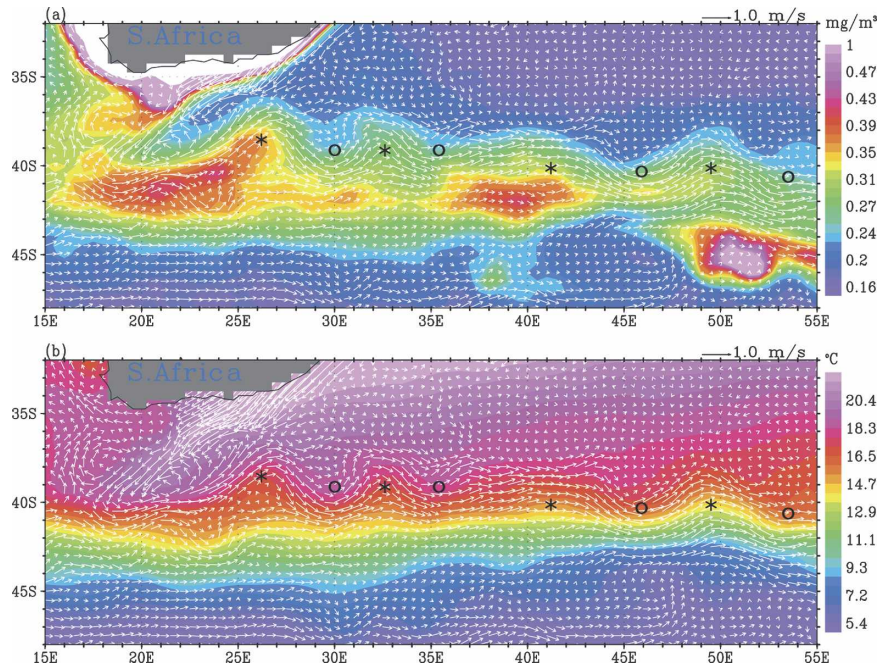


FIG. 2. Ocean surface current measured by Lagrangian drifters (white arrows) superimposed on (a) chlorophyll (color, mg m^{-3}) from SeaWiFS and (b) SST (color, $^{\circ}\text{C}$) from AMSR-E. Circles and stars represent centers of warm and cold SST anomalies.

clearly demonstrated in Fig. 5a. Positive ENW anomalies are found over warmer water and negative anomalies over cooler water. For example, at 26°E (location A) and 50.0°E (location B), negative ENW anomalies of 0.6 and 0.35 m s^{-1} correspond to negative SST anomalies of 1.2° and 1.0°C , respectively. At 30°E (location C) and 53°E (location D), positive ENW anomalies

of 0.35 and 0.2 m s^{-1} correspond to positive SST anomalies of 0.9° and 0.8°C , respectively.

To illustrate that the coherence between QuikSCAT measurements and SST is inherent in the definition of ENW (turbulent mixing theory), ENW is computed with the method described in section 2a, using a uniform wind speed of 7.5 m s^{-1} at 10 m , but using

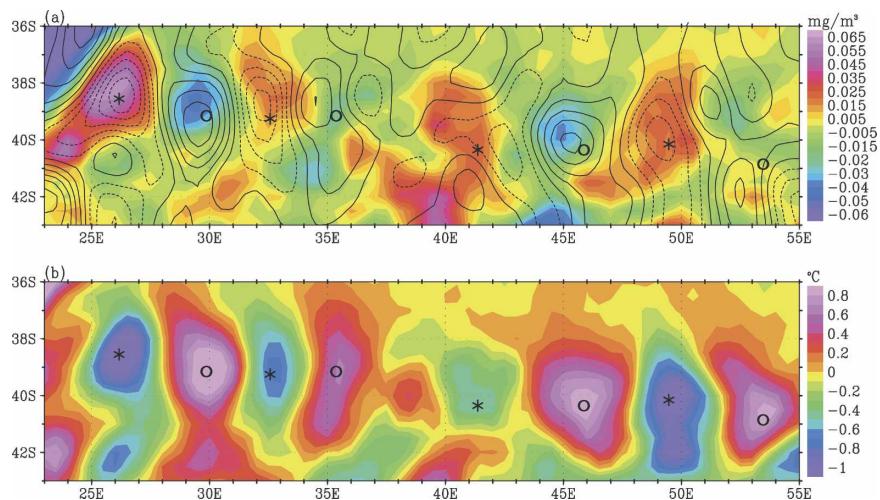


FIG. 3. Same as the color images in Fig. 2, except a two-dimensional filter has been applied. Contours of filtered ocean surface current vorticity are also shown in Fig. 3a; contour interval is $0.75 \times 10^{-6} \text{ s}^{-1}$.

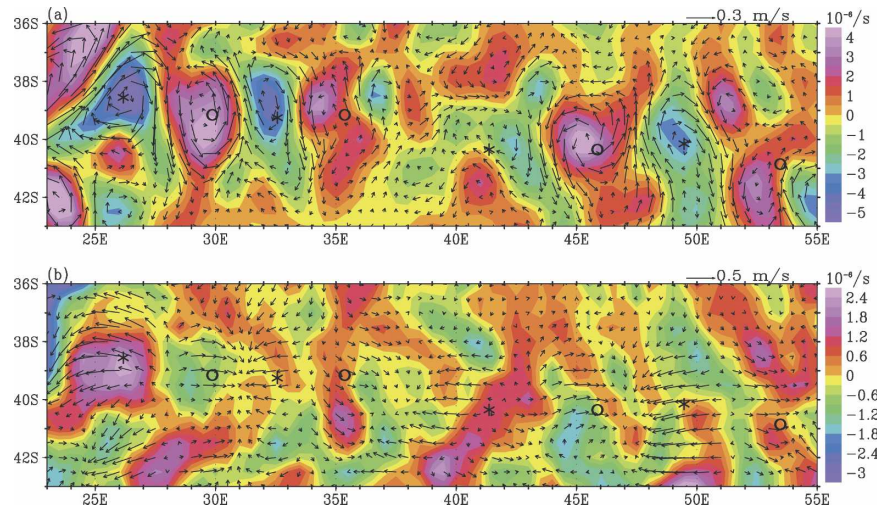


FIG. 4. (a) Filtered surface currents (black arrows) measured by drifters superimposed on the vorticity (color, 10^{-6} s^{-1}) derived from the current. (b) Filtered ENW measured by QuikSCAT superimposed on the vorticity (color, 10^{-6} s^{-1}) derived from ENW.

AMSR-E SST and NCEP air temperature and humidity at each grid location. The anomalies of ENW computed from a uniform wind speed field show similar coherence with SST as the QuikSCAT measurements (Fig. 5b). At location A and C in the west, the ENW anomalies with uniform wind speed account for about 30% of the anomalies measured by QuikSCAT and at location B and D in the east, they account for 90% of the SST-dependent anomalies observed by QuikSCAT.

The uniform wind speed we used is the average for both QuikSCAT and ECMWF (they are in close agree-

ment) for the region over the major eddies (37° – 42°S , 25° – 55°E) and for the period 2000–04. Using the higher wind speed from NCEP (9.7 m s^{-1}) would reduce the anomalies. Changes in wind speed or density stratification would, obviously, change the computed ENW contrasts across SST fronts as percentage of QuikSCAT observations, as discussed in more detail in section 4d. However, it is not the intention of this conceptual experiment to provide the exact quantitative portion of QuikSCAT wind anomalies represented by the present turbulence parameterization. The objective of this

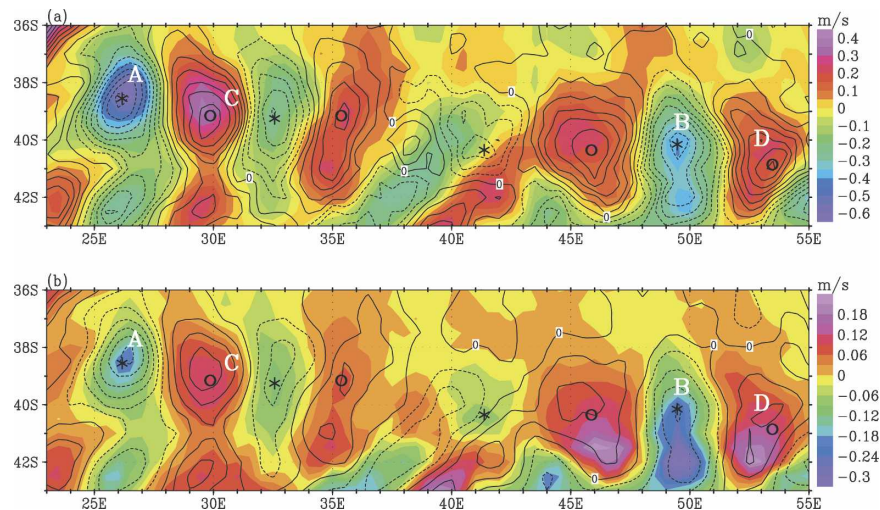


FIG. 5. (a) Filtered ENW magnitude (color, m s^{-1}) derived from QuikSCAT superimposed by SST (isotherms) from AMSR-E; isotherm interval is 0.15°C . (b) Filtered ENW magnitude computed using horizontally homogeneous wind speed (color, m s^{-1}) superimposed by QuikSCAT ENW magnitude (isotachs); isotach interval is 0.1 m s^{-1} .

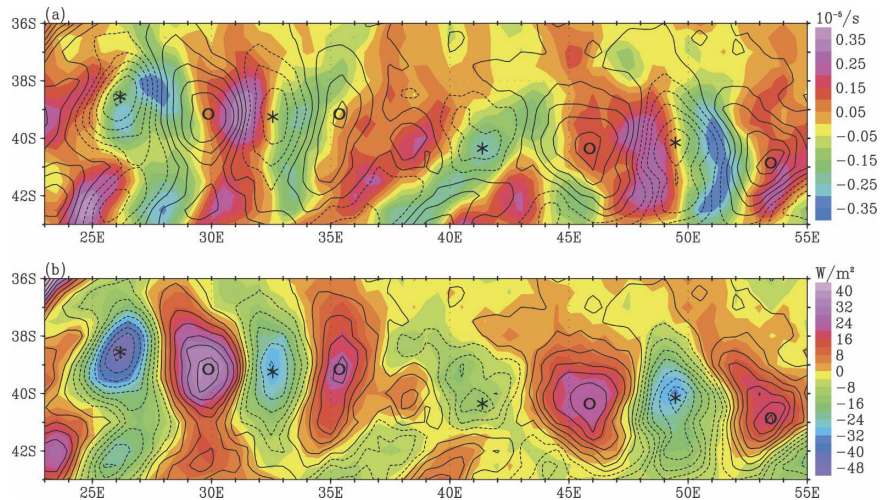


FIG. 6. (a) Filtered surface ENW convergence (color, 10^{-5} s^{-1}) and (b) latent heat flux (color, W m^{-2}), both superimposed by SST (isotherms). Isotherm interval is 0.15°C . The ENW convergence is derived from QuikSCAT, and latent heat flux is derived from AMSR-E.

study, as addressed in section 4d, is to show that the dependence of scatterometer observations on SST is an inherent characteristic of stress, and to explore the other possible causes of the ENW–SST coherence observed from QuikSCAT and AMSR-E if turbulent mixing alone could not account for the spatial coherence.

d. Surface convergence

Westerly ENW anomalies are collocated with warm SST anomalies, and easterlies are collocated with cold SST; the result is that spatial variation of surface ENW convergence is in quadrature (90° phase difference) with SST (Fig. 6a). The convergence on the downwind side of high SST anomalies is the result of the deceleration of ENW, and the divergence on the upwind side of the high SST anomalies is the result of acceleration of ENW. The convergence and divergence may result in ascending and descending air motion, respectively. The possible enhanced convection and feedback is discussed in section 4d.

e. Surface latent heat flux

Figure 6b shows that evaporative cooling is enhanced over areas of collocated warmer water and higher ENW and reduced over areas of lower SST and lower ENW. Typical time series were shown in Fig. 7a as an example, illustrating the positive contemporary correlation among the three parameters after filtering. Higher SST causes higher wind and evaporation almost instantaneously. The filtering, in effect, removes the low-frequency variation (annual cycle). Without filtering, however, the annual cycle dominates (Fig. 7b). Evapo-

ration is opposite in phase with the temporal rate of change of SST, which is in quadrature with SST itself. Higher wind speed and higher evaporation during winter start the cooling, which results in the lowest SST occurring a few months later. The contemporary correlation between wind speed and SST will be negative, as described in previous studies over global ocean (e.g., Liu et al. 1994). More explanations and implications are given in section 4c.

f. Upper atmosphere signatures

Figure 8a shows that, averaged over the same 5-yr period, the ISCCP CTT anomalies have a similar distribution as SST anomalies. Clear-sky pixels were removed in this dataset to eliminate the influence by surface temperature. Figure 8b shows that optically thicker clouds are observed to be collocated with higher CTT and SST and vice versa. Cloud-top pressure from ISCCP data varies from 570 mb over the cold eddies (e.g., 26°E) to 650 mb over the warm eddies (e.g., 30°E), but the values are derived from the temperature field based on knowledge of the atmospheric temperature profile and are not directly observed from space-based sensors. Nonetheless, it implies that the cloud top is high above the usual height of atmospheric boundary layer (900 mb). The collocation of CTT and SST anomalies indicates interaction between SST and the atmosphere way above the atmospheric boundary layer.

AIRS temperature soundings show that the high- and low-temperature anomalies, collocated with warm and cold ocean eddies, penetrate all the way up to 300 mb,

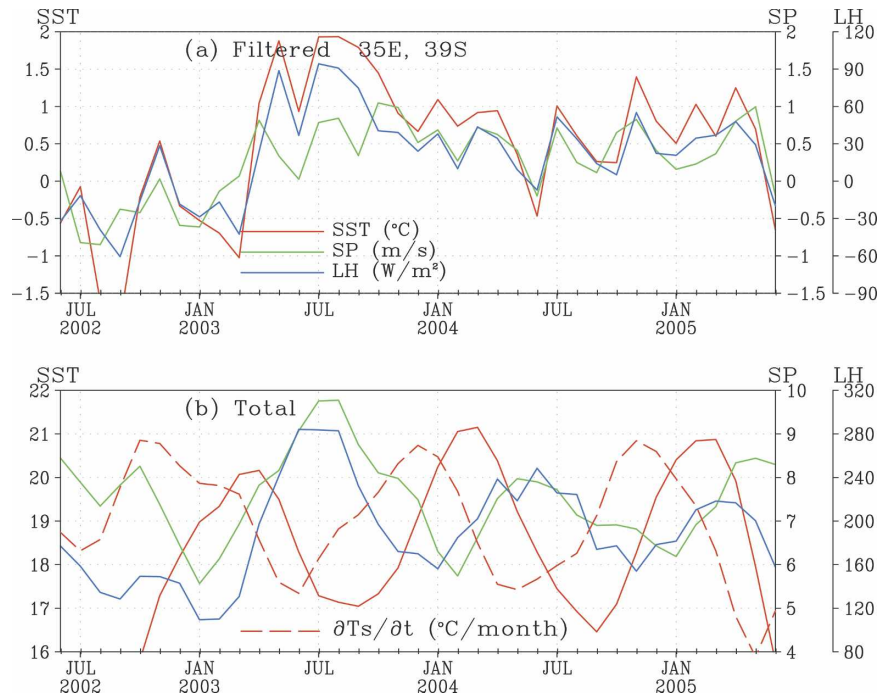


FIG. 7. Time series of monthly SST (red curve), surface wind speed (green curve), and latent heat flux (blue curve) at 39°S, 35°E. SST and latent heat flux are derived from AMSR-E and wind speed from QuikSCAT. (a) Filtered data and (b) unfiltered data with a 3-month running mean.

as represented by the cross section along 40°S shown in Fig. 9. Divakarla et al. (2006) showed that the random error of AIRS measurement over ocean, as represented by the global root-mean-square differences between instantaneous AIRS temperature and radiosonde profile,

is about 1°C for each 1-km layer. Temporal averaging will reduce the random errors by a factor equal to the square root of the degree of freedom. Assuming a decorrelation time scale of 5 days, the 3-yr average profile will reduce random errors to 1/14 times of 1°C (0.07°C).

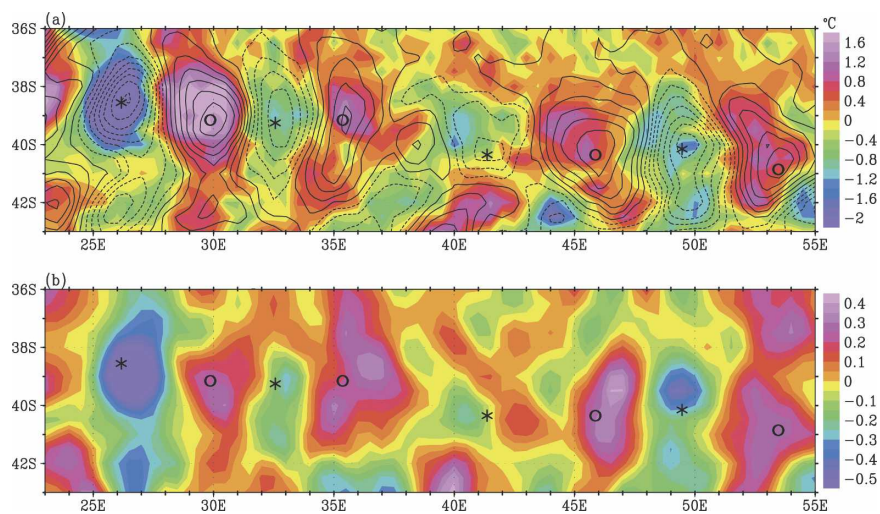


FIG. 8. (a) Filtered CTT (color, °C) derived from ISCCP superimposed by SST from AMSR-E (isotherms). Isotherm interval is 0.15°C. (b) Filtered cloud optical thickness from ISCCP.

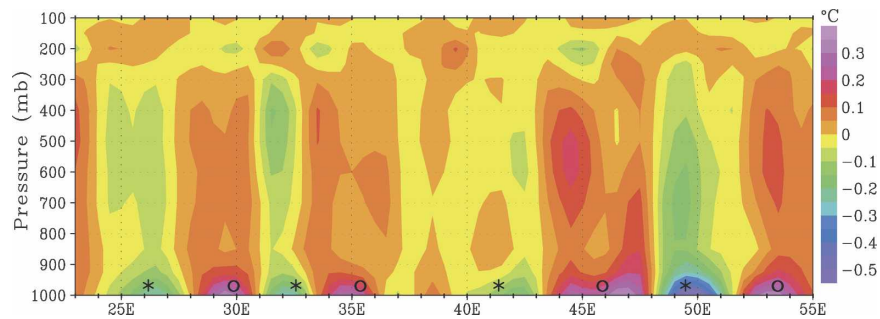


FIG. 9. Vertical structure of filtered air temperature ($^{\circ}\text{C}$) across 40°S from AIRS data. Circles and stars are projected locations of the SST anomaly centers shown in Fig. 2b.

Even with a 10-day decorrelation time scale, the accuracy will still be better than 0.1°C . The $0.1^{\circ}\text{--}0.2^{\circ}\text{C}$ anomalies shown in Fig. 9 are significant. Tian et al. (2006) demonstrated that AIRS temperature anomalies of similar magnitude could be successfully used to study Madden-Julian oscillation.

The correlation coefficients of the geographic variations (585 pairs of data at a 0.5° grid in the region of $42^{\circ}\text{--}38^{\circ}\text{S}$, $23^{\circ}\text{--}55^{\circ}\text{E}$) between SST and CTT for 3-yr, 1-yr, and 3-month periods are nearly constant, over 0.7; they decrease to around 0.65, 0.5, and 0.4 at 1-month, 10-day, and 5-day periods, respectively. The correlation coefficients between SST and upper-level AIRS temperature (e.g., 600 mb) also decrease with shorter averaging periods, but with sharper drops at short periods, from over 0.6 at 1 yr to 0.15 at 5 days.

If one assumes 585/4 (every other grid point) as the degree of freedom, a correlation coefficient of 0.16 will meet the 95% confidence criterion. If we use 585/9 (every third grid point) as the degree of freedom, a correlation coefficient of 0.24 will meet the 95% confident level. An additional significance test is performed using Monte Carlo simulation. The 585 pairs of data were selected randomly from all 10-day and monthly averages separately, and the correlation coefficients were computed repeatedly 1000 times to obtain a normal distribution. In both cases, the 95% confidence level is 0.085. Except for the time period of 5 days and shorter (synoptic time scales) the spatial correlations are significant.

4. Discussions

a. Ocean dynamics

The AMSR-E SST and SeaWiFS chlorophyll clearly support the identification of the AEC semipermanent meanders by Lagrangian drifters. The locations of the anomalies are in agreement with the short-duration

cruise measurements during the Cape of Good Hope Experiments (KAPEX; Boebel et al. 2003), which are largely made in the western region. When compared with drifter measurements averaged for the previous 5 yr (January 1995 to December 1999), the locations of the eddies west of 35°E remain unchanged, while the locations of the eastern eddies are less well defined. The agreement at different time periods demonstrates the quasi-steady nature of the meandering jets, first identified by Pazan and Niiler (2004) using drifter measurements from 1978 to 2003.

The dynamic balance of similar quasi-steady fronts has been postulated by Niiler et al. (2003), Hughes (2005), and Ochoa and Niiler (2007). While the zonal orientation of chlorophyll concentration in the Circumpolar Current observed by SeaWiFS has been investigated (e.g., Moore and Abbott 2000; Pollard et al. 2002), the strong chlorophyll concentration poleward of the maximum AEC current, as shown in Fig. 2, has not been discussed and the mechanism of its formation, whether it is due to horizontal transport or upwelling, is unknown.

b. Feedback on current

As explained in section 2a, τ depends on wind shear, or the difference between the wind vector near the surface and the surface current. The importance of surface current feedback on the determination of stress in the tropical ocean was studied by simulation using ocean general circulation models (e.g., Pacanowski 1987). While surface current has been included in some of the formulation of bulk parameterization of stress (e.g., Liu et al. 1979), it is generally assumed to be negligible compared with wind. Scatterometer data show that such assumption is not valid when the magnitude of wind relative to current is low, as over tropical oceans (Kelly et al. 2001), and when there is directional difference caused by current rotation. Because ocean surface

current is not used as boundary conditions, NWP data could not produce the rotation τ with the current effect.

The rotation of ENW in opposition to the rotation of the surface current observed over the AEC is in agreement with the observation of Cornillon and Park (2001) over the Gulf Stream rings. It clearly demonstrates that the scatterometer measures stress rather than winds. The opposite sign of the vorticity also implies that the stress anomalies spin down the current rotation through momentum transport. The small magnitude of ENW vorticity anomalies compared with those of the ocean current anomalies implies that ocean current dominates in the long-term mesoscale vorticity coupling.

The ENW vorticity anomalies (Fig. 4b) are collocated (and opposite in phase) with ocean current and SST anomalies; they should be in quadrature with the vorticity caused by the crosswind SST gradient described in the introduction. O'Neill et al. (2005), using a broader filter, show the in-phase correlation between ENW vorticity and crosswind SST gradient over a larger region that includes the entire Agulhas Current system and circumpolar currents. However, over the smaller region we examined (38° – 41° S, 25° – 37° E), both O'Neill's and our results show that the correlation between ENW vorticity and crosswind SST gradient is weak and the effect of surface current vorticity on ENW vorticity dominates.

c. Feedback on ocean temperature

The latent heat flux, as represented by conventional bulk parameterization, is

$$\text{LH} = \rho_a C_e L u [Q(T_s) - rQ(T_s - \Delta T)],$$

where L is the latent heat of vaporization, ρ_a is surface air density, C_e is the water vapor transfer coefficient, r is the relative humidity, T_s is SST, ΔT is sea–air temperature difference, and $Q(T)$ is the saturation specific humidity at temperature T . Atmospheric turbulent mixing is fast. The temporal variation of LH, u , and T_s are in phase. The contemporary positive correlations among the filtered SST, u , and LH over the mesoscale eddies are the result of the ocean driving the atmosphere.

A simplified representation of the heat balance in a well-mixed layer of the upper ocean of depth h with temperature approximately equal to T_s is

$$\rho_w c h \frac{\partial T_s}{\partial t} = A - \text{LH},$$

where ρ_w is the surface water density, c is isobaric specific heat of water, and A is the sum of ocean heat advection (horizontal and vertical), the surface radiative flux, and sensible heat flux into the layer. The time series in Fig. 7b shows the atmosphere driving the ocean. While the variation of LH is opposite in phase with $\partial T_s / \partial t$, it is in quadrature with T_s (sine and cosine functions). If the temporal variation is dominated by the annual cycle, T_s may lag LH by a season. It takes time for LH to cool the ocean surface layer. Figure 7b shows that the low SST lags the high wind and high latent heat flux, and this negative correlation between wind speed and SST is prevalent if the low-frequency variation is retained. The results are consistent with the analysis of large-scale and low-frequency variations over the global ocean using space-based data by Liu et al. (1994). Another major factor is the solar heating; its annual variation is shown by Liu et al. (1994) to be in phase with $\partial T_s / \partial t$. How the mesoscale variation of evaporation affects low-frequency variation or atmospheric buoyancy and convection remains to be ascertained.

d. Feedback on stress

The spatial coherence of SST with ENW both measured by QuikSCAT and computed in our conceptual experiment of horizontally homogeneous wind speed, supports that QuikSCAT measures stress rather than wind. If the spatial coherence between scatterometer observations and SST is mainly caused by the dependence of turbulent mixing with atmospheric density stratification, as postulated by almost all the past studies (cited in the introduction), the coherence should be inherent in the definition of ENW. Any discrepancies, if realistic, may suggest the present scatterometer model function does not accurately retrieve ENW or the need of additional positive feedback to the turbulent mixing mechanism.

Unfortunately, high-resolution atmospheric temperature and humidity measurements are not available to derive the stability parameters and ascertain the discrepancies in the conceptual experiment; NCEP temperature and humidity may not sufficiently represent the long-term, high-resolution features over AEC. The winds should not be spatially uniform, but constantly adjusting to the ocean fronts, through turbulent transport and response to large-scale thermodynamics. The computed ENW, of course, depends on the stability function ψ , which represents the state-of-art knowledge of turbulence parameterization. Although there have been many investigations to improve the drag coefficient (e.g., Fairall et al. 1996) in past few decades, there is no significant change in the formulation of ψ .

There are various error sources for ENW related to SST. The model function might be calibrated not against ENW but the actual winds. Except for the pre-flight model function for the NASA Scatterometer (NSCAT) [called Seasat-A Satellite Scatterometer (SASS-2)], which was adjusted with ENW computed from in situ measurements (e.g., JASIN experiment) collected for *Seasat* validation, most tuning of revised model functions (e.g., NSCAT-1, NSCAT-2) was based on NWP wind products (e.g., Wentz and Smith 1999) that are not ENW. ENW errors depend on the history of calibration and are difficult to gauge. Surface stress (or ENW) depends on surface viscosity, which varies with SST. A small secondary effect of stress dependence on viscosity at weak winds was observed by Liu (1984), in agreement with postulation of Leonart and Blackman (1980). According to the postulation, the backscatter coefficient and ENW would be higher at higher viscosity and lower SST, in opposite to the observed relation between ENW and SST presented in section 3c.

Turbulent mixing may not be able to account for all the ENW or stress anomalies related to SST. Convective mixing may be the additional mechanism to enhance the horizontal stress anomalies across the temperature front. QuikSCAT observations show that the variation of ENW divergence anomalies are in quadrature with SST similar to the results of Xie et al. (1998) and Liu et al. (2000), in the tropical Pacific, or in phase with downwind temperature gradient as described by Chelton et al. (2001). As illustrated in Fig. 6a, convergence found on the downwind side of local SST maxima may result in ascending air and divergence on the upwind side may result in descending air, reversed divergence and vertical motions on the two sides of SST minima. The result of the convective cell may be a positive feedback to the ENW–SST coherence resulting from stability difference; it accelerates ENW over warm water and decelerates ENW over cool water. The question is how high does such convection go over a long period of time.

e. Possible effect on upper troposphere

Past studies of atmospheric responses to ocean thermal fronts, whether through observations or numerical experiments, explored only the limited effects on the atmospheric boundary layer. Strong synoptic variability and atmospheric forcing are believed to be more important than ocean forcing in the midlatitudes. The AIRS soundings and ISCCP data show that the thermal effect extends far above the boundary layer. It is apparent that the whole atmosphere warms and forms

optically thicker clouds over warmer water and cools and forms optically thinner clouds over cooler water. Accurate measurement of vertical velocity is not available to examine the dynamics. The dynamics and thermodynamics of such behavior need to be addressed in future study. There is likely to be significant cloud–SST feedback (Ramanathan and Collins 1991; Fu et al. 1996; Lin et al. 2002) that also requires further investigation. The high-resolution ECMWF and NCEP vertical temperature profiles do not show the penetrating temperature effects as in the AIRS soundings. It is questionable whether the operational atmospheric models have sufficient mesoscale thermodynamics to produce realistic long-term means.

5. Conclusions

The recent push from research to operational applications of a space-based scatterometer has channeled much community effort in articulating scatterometer as a wind-measuring instrument for operational numerical weather and tropical cyclone predictions. The original justification for the scatterometer, however, came from oceanographers who need surface wind forcing of the ocean (O'Brien 1982). Ocean surface stress, rather than wind, is the momentum flux, which drives ocean circulation that affects long-term climate changes. This study clarifies the unique capability of the scatterometer in measuring stress over global ocean, night and day, clear and cloudy, at high spatial resolution. The dependence of scatterometer measurements on ocean surface current and SST should not be viewed as wind error or wind anomalies but as the natural characteristics of surface stress. For a long time, stress has been derived only from wind, and its dependence on ocean variability has mostly been neglected. Scatterometer measurements are casting new light on stress and will improve future research and operational, meteorological, and oceanic applications.

There has been continuous improvement in the spatial resolution of NWP outputs. The use of high-resolution SST as boundary condition (starting May 2001 at ECMWF) and the assimilation of QuikSCAT data (starting in January 2002 for both NCEP and ECMWF) should have improved the operational surface wind products. But without inputs of ocean parameters, such as surface currents, surface waves, and sea state, improving stress estimation would be difficult. Our present parameterization of stress in terms of wind is not sufficient over ocean fronts, and perhaps, in severe storms. Direct measurements of stress from spaceborne scatterometers, without the need of deriving it from the wind vector, are critically needed.

The Agulhas Currents continuously supply energy to maintain the current shears and surface temperature gradients that cause the instability in the atmosphere and generate turbulent mixing. Atmospheric turbulence tends to dissipate the energy, reduces the instability, and provides a negative feedback to smooth out the ocean gradients. In the atmosphere, the effect of ocean fronts may include positive feedback on convective mixing that enhances the horizontal stress gradient. Dynamic linkage of surface turbulent transfer to large-scale circulation and cloud–radiative feedback, in the future, will require multi-year and high-resolution data with sufficient coverage from a combination of space-based sensors.

Experimental investigation of air–sea interaction near ocean fronts has been mostly on synoptic time scales and within the boundary layer; the validations of space-based observations are mostly made at synoptic time scales. The results of this study show potential effects of surface anomalies near the ocean front, in long periods and high into the atmosphere; the effects are important to climate changes and radiation balance in the atmosphere. Present NWP models may not have the physics to simulate the long-term, penetrating effects, making space-based observations (e.g., ISCCP and AIRS) all the more important in the characterization, understanding, and prediction of climate changes. This study demonstrates the synergism of five sets of space-based measurements, QuikSCAT, AMSR-E, SeaWiFS, AIRS, and ISCCP and the surface current measured by the Lagrangian drifters.

Acknowledgments. This study was conducted at the Jet Propulsion Laboratory, California Institute of Technology, under contract of NASA. It was jointly supported by the Physical Oceanography, Ocean Vector Wind, Earth Observing System, and the Energy and Water Cycle Programs of NASA. William Rossow, Eric Fetzer, Hartmut Aumann, and Moustafa Chahine kindly reviewed and advised on the analyses of ISCCP and AIRS data.

REFERENCES

- Boebel, O., T. Rossby, J. Lutjeharms, W. Zenk, and C. Barron, 2003: Path and variability of the Agulhas Return Current. *Deep-Sea Res. II*, **50**, 35–56.
- Brown, R. A., and W. T. Liu, 1982: An operational large-scale marine planetary boundary layer model. *J. Appl. Meteor.*, **21**, 261–269.
- Chahine, M. T., and Coauthors, 2006: AIRS: Improving weather forecasting and providing new data on greenhouse gases. *Bull. Amer. Meteor. Soc.*, **87**, 911–926.
- Chelton, D. B., and Coauthors, 2001: Observations of coupling between surface wind stress and sea surface temperature in the eastern tropical Pacific. *J. Climate*, **14**, 1479–1498.
- , M. G. Schlax, M. H. Freilich, and R. Milliff, 2004: Satellite measurements reveal persistent small-scale features in ocean winds. *Science*, **303**, 978–983.
- Cornillon, P., and K.-A. Park, 2001: Warm core ring velocities inferred from NSCAT. *Geophys. Res. Lett.*, **28**, 575–578.
- Cronin, M. F., S.-P. Xie, and H. Hashizume, 2003: Barometric pressure variations associated with eastern Pacific tropical instability waves. *J. Climate*, **16**, 3050–3057.
- Divakarla, M. G., C. D. Barnett, M. D. Goldberg, L. M. McMillin, E. Maddy, W. Wolf, L. Zhou, and X. Liu, 2006: Validation of Atmospheric Infrared Sounder temperature and water vapor retrievals with matched radiosonde measurements and forecasts. *J. Geophys. Res.*, **111**, D09S15, doi:10.1029/2005JD006116.
- Fairall, C. W., E. F. Bradley, D. P. Rogers, J. B. Edson, and G. S. Young, 1996: Bulk parameterization of air–sea fluxes for Tropical Ocean–Global Atmosphere Coupled Ocean–Atmosphere Response Experiment. *J. Geophys. Res.*, **101**, 3747–3764.
- Fleagle, R. G., and J. A. Businger, 1963: *An Introduction to Atmospheric Physics*. Academic Press, 346 pp.
- Friehe, C. A., and Coauthors, 1991: Air–sea fluxes and surface layer turbulence around a sea surface temperature front. *J. Geophys. Res.*, **96** (C5), 8593–8609.
- Fu, R., W. T. Liu, and R. E. Dickinson, 1996: Response of tropical clouds to the interannual variation of sea surface temperature. *J. Climate*, **9**, 616–634.
- Geernaert, G., 1990: Bulk parameterizations for the wind stress and heat fluxes. *Current Theory*, G. Geernaert and W. J. Plant, Eds., Vol. 1, *Surface Waves and Fluxes*, Kluwer Academic, 91–172.
- Greenhut, G. K., 1982: Stability dependence of fluxes and bulk transfer coefficients in a tropical boundary layer. *Bound.-Layer Meteor.*, **24**, 253–264.
- Guymer, T. H., J. A. Businger, K. B. Katsaros, W. J. Shaw, P. K. Taylor, W. G. Large, and R. E. Payne, 1983: Transfer processes at the air–sea interface. *Philos. Trans. Roy. Soc. London*, **A308**, 253–273.
- Hashizume, H., S.-P. Xie, M. Fujiwara, M. Shiotani, T. Watanabe, Y. Tanimoto, W. T. Liu, and K. Takeuchi, 2002: Direct observations of atmospheric boundary layer response to SST variations associated with tropical instability waves over the eastern equatorial Pacific. *J. Climate*, **15**, 3379–3393.
- Hayes, S. P., M. J. McPhaden, and J. M. Wallace, 1989: The influence of sea-surface temperature on surface wind in the eastern equatorial Pacific: Weekly to monthly variability. *J. Climate*, **2**, 1500–1506.
- Hughes, C. W., 2005: Nonlinear vorticity balance of the Antarctic Circumpolar Current. *J. Geophys. Res.*, **110**, C11008, doi:10.1029/2004JC002753.
- Kelly, K. A., S. Dickinson, M. J. McPhaden, and G. C. Johnson, 2001: Ocean currents evident in satellite wind data. *Geophys. Res. Lett.*, **28**, 2469–2472.
- Kushnir, Y., W. A. Robinson, I. Bladé, N. M. J. Hall, S. Peng, and R. Sutton, 2002: Atmospheric GCM response to extratropical SST anomalies: Synthesis and evaluation. *J. Climate*, **15**, 2233–2256.
- Lau, N.-C., and M. J. Nath, 1994: A modeling study of the relative roles of tropical and extratropical SST anomalies in the variability of the global atmosphere–ocean system. *J. Climate*, **7**, 1184–1207.
- Lin, B., B. Wielicki, L. Chambers, Y. Hu, and K.-M. Xu, 2002: The

- iris hypothesis: A negative or positive cloud feedback? *J. Climate*, **15**, 3–7.
- Lin, I.-I., W. T. Liu, C.-C. Wu, J. C. H. Chiang, and C.-H. Sui, 2003: Satellite observations of modulation of surface winds by typhoon-induced upper ocean cooling. *Geophys. Res. Lett.*, **30**, 1131, doi:10.1029/2002GL015674.
- Liu, W. T., 1984: The effects of the variations in sea surface temperature and atmospheric stability in the estimation of average wind speed by SEASAT-SASS. *J. Phys. Oceanogr.*, **14**, 392–401.
- , 2002: Progress in scatterometer application. *J. Oceanogr.*, **58**, 121–136.
- , and W. G. Large, 1981: Determination of surface stress by Seasat-SASS: A case study with JASIN data. *J. Phys. Oceanogr.*, **11**, 1603–1611.
- , and W. Tang, 1996: Equivalent neutral wind. JPL Publication 96-17, Jet Propulsion Laboratory, California Institute of Technology, Pasadena, CA, 16 pp.
- , and X. Xie, 2002: Double intertropical convergence zones—A new look using scatterometer. *Geophys. Res. Lett.*, **29**, 2072, doi:10.1029/2002GL015431.
- , and —, 2006: Measuring ocean surface wind from space. *Remote Sensing of Human Settlements*, M. K. Ridd and J. D. Hipple, Eds., Manual of Remote Sensing, Vol. 5, American Society for Photogrammetry and Remote Sensing, 149–178.
- , K. B. Katsaros, and J. A. Businger, 1979: Bulk parameterization of air-sea exchanges of heat and water vapor including the molecular constraints at the interface. *J. Atmos. Sci.*, **36**, 1722–1735.
- , W. Tang, and P. P. Niiler, 1991: Humidity profiles over the ocean. *J. Climate*, **4**, 1023–1034.
- , A. Zhang, and J. Bishop, 1994: Evaporation and solar irradiance as regulators of sea surface temperature in annual and interannual changes. *J. Geophys. Res.*, **99**, 12 623–12 638.
- , W. Tang, and R. Atlas, 1996: Responses of the tropical Pacific to wind forcing as observed by spaceborne sensors and simulated by an ocean general circulation model. *J. Geophys. Res.*, **101**, 16 345–16 360.
- , X. Xie, P. S. Polito, S.-P. Xie, and H. Hashizume, 2000: Atmospheric manifestation of tropical instability wave observed by QuikSCAT and Tropical Rain Measuring Mission. *Geophys. Res. Lett.*, **27**, 2545–2548.
- Liu, Z., and L. Wu, 2004: Atmospheric response to North Pacific SST: The role of ocean–atmosphere coupling. *J. Climate*, **17**, 1859–1882.
- Leonart, G. T., and D. R. Blackman, 1980: The spectral characteristics of wind-generated capillary waves. *J. Fluid Mech.*, **97**, 455–479.
- Luis, A. J., and P. C. Pandey, 2005: Characteristics of atmospheric divergence and convergence in the Indian Ocean inferred from scatterometer winds. *Remote Sens. Environ.*, **97**, 231–237.
- McClain, C. R., G. C. Feldman, and S. B. Hooker, 2004: An overview of the SeaWiFS project and strategies for producing a climate research quality global ocean bio-optical time series. *Deep-Sea Res. II*, **51**, 5–42.
- Moore, J. K., and M. R. Abbott, 2000: Phytoplankton chlorophyll distributions and primary production in the Southern Ocean. *J. Geophys. Res.*, **105**, 28 709–28 722.
- Niiler, P. P., 2001: The World Ocean surface circulation. *Ocean Circulation and Climate: Observing and Modelling the Global Ocean*, G. Siedler, J. Church, and J. Gould, Eds., International Geophysics Series, Vol. 77, Academic Press, 193–204.
- , N. A. Maximenko, and J. C. McWilliams, 2003: Dynamically balanced absolute sea level of the global ocean derived from near-surface velocity observations. *Geophys. Res. Lett.*, **30**, 2164, doi:10.1029/2003GL018628.
- Nonaka, M., and S.-P. Xie, 2003: Covariations of sea surface temperature and wind over the Kuroshio and its extension: Evidence for ocean-to-atmosphere feedback. *J. Climate*, **16**, 1404–1413.
- O'Brien, J. J., 1982: *Scientific Opportunities Using Satellite Surface Stress Measurements Over the Ocean—Report of the Satellite Surface Stress Working Group*. Nova University Press, 163 pp.
- Ochoa, J., and P. P. Niiler, 2007: Vertical vorticity balance in meanders downstream the Agulhas retroflection. *J. Phys. Oceanogr.*, **37**, 1740–1744.
- O'Neill, L. W., D. B. Chelton, and S. Esbensen, 2003: Observations of SST-induced perturbations of the wind stress field over the Southern Ocean on seasonal time scales. *J. Climate*, **16**, 2340–2354.
- , —, —, and F. J. Wentz, 2005: High-resolution satellite measurements of the atmospheric boundary layer response to SST variations along the Agulhas Return Current. *J. Climate*, **18**, 2706–2723.
- Pacanowski, R. C., 1987: Effect of equatorial currents on surface stress. *J. Phys. Oceanogr.*, **17**, 833–838.
- Park, K.-A., and P. Cornillon, 2002: Stability-induced modification of sea surface winds over Gulf Stream rings. *Geophys. Res. Lett.*, **29**, 2211, doi:10.1029/2001GL014236.
- Pazan, S. E., and P. P. Niiler, 2004: Ocean sciences: New global drifter data set available. *Eos, Trans. Amer. Geophys. Union*, **85**, 17.
- Polito, P. S., J. P. Ryan, W. T. Liu, and F. P. Chavez, 2001: Oceanic and atmospheric anomalies of tropical instability waves. *Geophys. Res. Lett.*, **28**, 2233–2236.
- Pollard, R. T., M. I. Lucas, and J. F. Read, 2002: Physical controls on biogeochemical zonation in the Southern Ocean. *Deep-Sea Res. II*, **49**, 3289–3305.
- Ramanathan, V., and W. Collins, 1991: Thermodynamic regulation of ocean warming by cirrus clouds deduced from observations of the 1987 El Niño. *Nature*, **351**, 27–32.
- Rossov, W. B., and R. A. Schiffer, 1999: Advances in understanding clouds from ISCCP. *Bull. Amer. Meteor. Soc.*, **80**, 2261–2287.
- Small, R. J., S.-P. Xie, and Y. Wang, 2003: Numerical simulation of atmospheric response to Pacific tropical instability waves. *J. Climate*, **16**, 3723–3741.
- Song, Q., T. Hara, P. Cornillon, and C. A. Friehe, 2004: A comparison between observations and MM5 simulations of the marine atmospheric boundary layer across a temperature front. *J. Atmos. Oceanic Technol.*, **21**, 170–178.
- Tennekes, H., and J. L. Lumley, 1972: *A First Course in Turbulence*. MIT Press, 300 pp.
- Tian, B., D. E. Waliser, E. J. Fetzer, B. H. Lambriksen, Y. L. Yung, and B. Wang, 2006: Vertical moist thermodynamic structure and spatial-temporal evolution of the MJO in AIRS observations. *J. Atmos. Sci.*, **63**, 2462–2485.
- Vecchi, G. A., S.-P. Xie, and A. S. Fischer, 2004: Ocean–atmosphere covariability in the western Arabian Sea. *J. Climate*, **17**, 1213–1224.
- Wentz, F. J., and D. K. Smith, 1999: A model function for the ocean-normalized radar cross section at 14 GHz derived from NSCAT observations. *J. Geophys. Res.*, **104**, 11 499–11 514.

- , and T. Meissner, 2000: Algorithm Theoretical Basis Document (ATBD) version 2: AMSR ocean algorithm. Remote Sensing Systems Tech. Rep. 121599A, 59 pp.
- , C. L. Gentemann, D. Smith, and D. Chelton, 2000: Satellite measurements of sea surface temperature through clouds. *Science*, **288**, 847–850.
- White, W. B., and J. L. Annis, 2003: Coupling of extratropical mesoscale eddies in the ocean to westerly winds in the atmospheric boundary layer. *J. Phys. Oceanogr.*, **33**, 1095–1107.
- Xie, S.-P., 2004: Satellite observations of cool ocean–atmosphere interaction. *Bull. Amer. Meteor. Soc.*, **85**, 195–208.
- , M. Ishiwatari, H. Hashizume, and K. Takeuchi, 1998: Coupled ocean-atmospheric waves on the equatorial front. *Geophys. Res. Lett.*, **25**, 3863–3866.
- , J. Hafner, Y. Tanimoto, W. T. Liu, H. Tokinaga, and H. Xu, 2002: Bathymetric effect on the winter sea surface temperature and climate of the Yellow and East China Seas. *Geophys. Res. Lett.*, **29**, 2228, doi:10.1029/2002GL015884.
- Yu, J.-Y., and W. T. Liu, 2003: A linear relationship between ENSO intensity and tropical instability wave activity in the eastern Pacific Ocean. *Geophys. Res. Lett.*, **30**, 1735, doi:10.1029/2003GL017176.